Reaction Kinetics and Temperature Effects in Syngas Photo-initiated Chemical Vapour Deposition on Single-Walled Carbon Nanotubes

Seyedehsan Hosseininasab [a], Nathalie Faucheux [b], Gervais Soucy [b] and Jason R. Tavares [a,*]

[a] *Department of Chemical Engineering, Polytechnique Montreal, Montreal, Québec H3T 1J4, Canada*

[b] *Department of Chemical and Biotechnological Engineering, Université de Sherbrooke, Sherbrooke, Québec J1K 2R1, Canada*

ABSTRACT

Photo-initiated chemical vapor deposition (PICVD) is a solvent-free process that can be used to produce thin films on a variety of substrates, with applications in fields ranging from biomedicine to optics and microelectronics. This study presents a kinetic analysis for this process using syngas ($CO+H_2$) as a precursor for the surface treatment of single walled carbon nanotubes (SWCNT) with average dimensions of 1.5×100 nm (diameter × length), and addresses the role of iron pentacarbonyl ($Fe(CO)_5$), a photo-active contaminant found in CO. This work builds upon previously-developed reaction schemes for PICVD, based mainly on surface characterizations, by coupling these analyses with gas-phase monitoring. This allows us to propose two separate reaction schemes for the gas and surface phase reactions and consider temperature effects. On-line FTIR, off-line GC-MS and on-line GC characterized the gas phase, while for surface characterizations, XPS and TGA were used. Characterizations showed that a coating with a general formula of $C_nO_{3n}Fe_n$ was deposited, corresponding to 0.29±0.04 mg carbon and 0.49±0.03 mg iron on the SWCNT substrate over the course of treatment. The $Fe(CO)_5$ was identified as the key reactant in syngas/PICVD reactions and was nearly completely consumed (94%). Mass balances derived from the gas phase characterization showed that $Fe(CO)_5$ inputted to the plug flow reactor could potentially contribute all the amount of 0.49±0.03 mg of Fe and 0.29±0.04 mg of C to the coating on the SWCNT, indicating that syngas/PICVD can be optimized in future to decrease gas throughput. Temperature did not show a significant effect in the case of PICVD.

However, in the absence of ultraviolet light, its role becomes determinant, with rising temperatures causing more Fe deposition.

KEYWORDS: PICVD; Photo-initiator; Coating; Iron Pentacarbonyl; Surface Treatment

1. Introduction

Chemical vapor deposition (CVD) is a process used in the semiconductor industry to produce thin films. The use of thin solid films is widespread - they are used in different technological areas such as microelectronics (integrated circuits, transistors), optical devices (laser, fibers), magnetic materials, solar energy conversion and ceramic industry (Dorval Dion et al. 2014). CVD can be classified into three major processes, namely thermally activated CVD (TACVD), plasma enhanced CVD (PECVD), and photo-initiated CVD (PICVD). In PICVD, chemical reactions are initiated by light photons (Dorval Dion et al. 2014; Farhanian et al. 2017) making use of various photo-sensitive precursors such as ethylene (C_2H_4) (Kasparek et al. 2016; Ruiz et al. 2010), butadiene ($C_4H_{6)}$ (Kasparek et al. 2016), hydrogen sulfide (H_2S) (Kasparek et al. 2016), ammonia (NH_3) (Girard-Lauriault et al. 2012), and ozone (O_3) (Raja 2014) to synthesize the desired coatings. For example, Kasparek et al. (2016) co-polymerized a gas mixture of ethylene/butadiene with hydrogen sulfide (H_2S) to obtain thiol-terminated thin films under vacuum-ultraviolet (VUV) irradiation (Kasparek et al. 2016). Precursor selection depends on the desired film properties and the available excitation wavelength of the light source (Choy 2003). The resulting film features are affected by kinetic and operational parameters such as choice of precursors, their respective flow rates (and molar ratio), their residence time in the system, the total pressure in the reactor, and the substrate temperature (Andrzejewska 2001b; Choy 2003). In particular, residence time can be directly related to other processing parameters such as treatment time, sample position inside the reactor and total flow rate of precursors, namely when using syngas ($CO+H_2$) as the precursor (syngas/PICVD or PICVD) (Hosseininasab et al. 2017). PICVD has demonstrated wide potential as a solvent-free surface engineering tool, able to deposit coatings and treat various surface

geometries (nanoparticles to flat substrates) under ambient conditions. This ability to operate at or near atmospheric pressure simplifies implementation, but complexifies the chemistry, as various simultaneous and interdependent processes take place, including homogeneous gas phase reactions (leading to reactive species formation), transport of these reactive species to the surface by passing the boundary layer, chemisorption/physisorption and desorption at the substrate surface, and heterogeneous reactions on the substrate yielding a solid functional deposit. This complexity is compounded by the presence of unexpected compounds, such iron pentacarbonyl ($Fe(CO)_5$), a photo-active contaminant found in CO (Nasri Lari et al. 2017).

$Fe(CO)_5$ forms over time inside steel CO cylinders, through a reaction with the cylinder wall at high-pressure (Williams and Shaddix 2007). Its absorption cross section peaks at wavelengths between 200 and 350 nm (Kotzian et al. 1989), meaning that it is readily dissociated by the light emitted by low-pressure Hg discharge germicidal ultraviolet C (UVC) lamps used in recent PICVD work to form reactive intermediates (Kotzian et al. 1989; Seder et al. 1986a). The thermal decomposition of $Fe(CO)_5$ is reported between 160 and 300 °C and forms Fe (III) oxide intermediates and iron oxide particles (Fondell et al. 2015; Wang et al. 2013). Our group previously suggested a preliminary kinetic model for PICVD based on surface characterizations (Dorval Dion et al. 2014; Farhanian et al. 2017). Dion et al. (2014) applied PICVD to functionalize flat surfaces under UVC light (253.7 nm) and they proposed a set of kinetic reactions based on Fischer–Tropsch synthesis (Dorval Dion et al. 2014). In their kinetic model, CO and H_2 played the leading roles and the $Fe(CO)_5$ contribution was not considered. Farhanian et al. (2017) further detailed the reaction kinetics when treating silicon substrates - although $Fe(CO)_5$ was considered in this kinetic model, the growth and termination reactions were mostly based on CO and H_2 (Farhanian et al. 2017). Considering the fact that syngas/PICVD is a flexible and promising method to change the surface properties of nanomaterials, it is necessary to clarify the reaction mechanisms at play for process scale-up to be eventually considered.

Our previous work (Hosseininasab et al. 2017) aimed to tailor the surface properties of single-wall carbon nanotubes (SWCNTs) using PICVD, as these fascinating materials have various applications exploiting their unique properties (such as high electrical conductivity and tensile strength (Lee et al. 2001)), but require surface modification for example to alter their wettability to facilitate their use in polar media (a key requirement

for biomedical applications). Given the potential of these nanomaterials, and the need to improve our understanding of the PICVD process, the present work deals with the in-depth kinetic modeling of PICVD considering both gas and surface phase reactions, as well as temperature effects on the functionalization of SWCNTs. To see how temperature affects precursor concentrations and deposition rates, we also investigated the functionalization of SWCNTs with TACVD, in which the light excitation of PICVD is replaced by heating. In the proposed model, we considered various kinetic parameters such as reaction rate of $Fe(CO)_5$ and temperature. The kinetic parameters are obtained experimentally.

2. Materials and Methods

2.1. Materials

Pure SWCNTs (P-SWCNTs) (96.5% w/w), syngas (CO and H_2, 99.97%), argon (99.9%) and hydrogen peroxide (H_2O_2, 50% (w/w)), were purchased from Raymor-NanoIntegris, Air Liquide, and Fisher Scientific (Montreal, Quebec), respectively. Liquid iron pentacarbonyl ($Fe(CO)_5$, >99.99%) was purchased from Sigma-Aldrich. CO and CO_2 calibration gas cylinders were purchased from Air Liquide. Two 96 cm-long UVC germicidal lamps (Model T-97505-80, Cole-Parmer Inc, low pressure Hg discharge, irradiance of 0.01 W/cm^2 at 3.5 cm) with the main and minor emission peaks at 253.7 and 185 nm, respectively, were used for all experimental treatments.

2.2. Experimental Procedures and Conditions

The PICVD reactor used in this study consisted of a 25-mm internal diameter quartz tube reactor illuminated by two UVC lamps, with gas flow supplied through three mass flow controllers (Brooks, series 5850E) and a syringe pump for photo-initiator (PI) injection (Fig.1) (Hosseininasab et al. 2017). SWCNT samples to be treated (in the form of bucky paper) were placed 30 cm from the reactor inlet, on a sample holder held at 45° with respect to the gas flow. After purging the reactor with argon, CO (containing traces of $Fe(CO)_5$, evaluated at 6.7±0.2 ppm/min, Fig. S1 in supplementary results) and

H_2 were injected with a molar ratio of 0.12 and a total flow of 400 ml/min. Hydrogen peroxide was continuously injected at a flow rate of 1 mL/h flow rate during the treatment. Except when otherwise specified, all surfaces were treated for 60 min under a pressure of 18.5 kPa (gauge pressure). Various temperatures (25-200 ºC) were applied to the sample holder, using a built-in electrical heater. A thermocouple was located right below the sample to monitor the temperature. In the course of this study, error bars (±) represent the standard deviation.

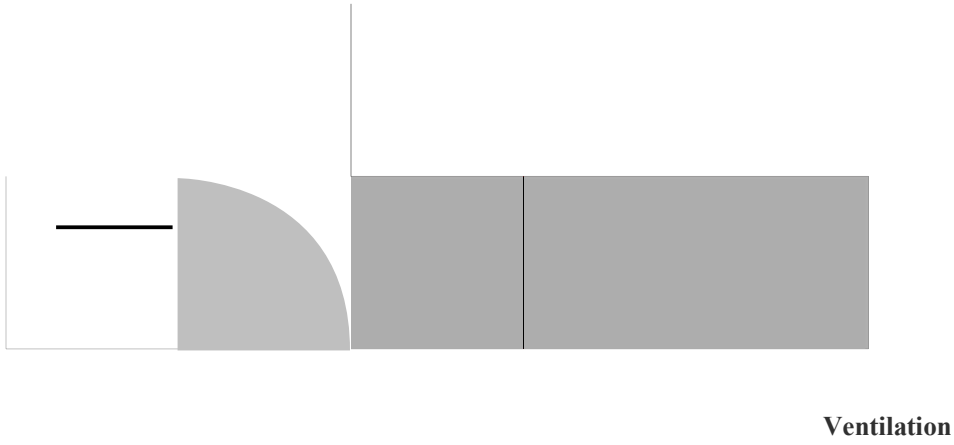

Fig. 1. Schematic of the PICVD reactor.

2.3. Surface and Gas Phase Characterization

The outlet gas (composed mainly of CO, H_2 and $Fe(CO)_5$) were analyzed with a Nicolet iS5 Fourier Transform Infrared (FT-IR) spectrometer operated in transmission mode with a quartz flow cell (Pike). Each spectrum is the result of 256 scans ranging from 500 to 4000 cm^{-1} at resolutions of 16 cm^{-1}. Gas chromatography mass spectroscopy (GC-MS) (Agilent 5975C VL MSD Triple Axis) equipped with two columns (Molsieve 5A and HayeSep N columns, California, USA) characterized gas samples. For CO and CO_2

quantifications, the HayeSep N column (80/100 Mesh 0.5m×1.8” IS) was used, while less stable components such as organic materials or $Fe(CO)_5$ were characterized with the Molsieve 5A column (13×80/100 Mesh 1.5m×1/8” IS). Helium served as carrier gas (flow rate of 0.5 mL/min). The gas samples analyzed were collected from the PICVD reactor using a Tedlar bag. For $Fe(CO)_5$ quantifications, 10 µl volume samples were injected to the GC-MS, while in the case of CO/CO_2, the column was first purged and then filled by the sample. The oven temperature had an isotherm at 45 °C for 20 min, and then increased linearly from 45 to 230 °C, until a total analysis time of 90 min was reached. Three $Fe(CO)_5$ samples diluted in toluene with concentrations of 0.1, 0.5, and 100 ppm were used for calibration of the GC-MS signal (Fig. S1, supplementary information). Here, based on the NIST 2010 library, components with a quality percentage over 90% are identified and reported (P. J. Linstrom and Mallard 2001) . To further quantify H_2, CO, O_2, N_2, C_2-C_4 hydrocarbons and CO_2, micro-gas chromatography (Varian CP-4900 Micro Gas Chromatograph) was used as well.

All treated samples (SWCNT sheets) were characterized via X-ray photoelectron spectroscopy (XPS) (VG ESCALAB 3 MKII system using a Mg Kα source), with 100 eV pass energy in 1 eV energy step size applied for survey scans. To obtain more insight into the composition of treated samples, high-resolution (HR) spectra were collected, with 20 eV pass energy in 0.05 eV increments. All peaks were fitted as per Yang and Sacher’s approach (Yang and Sacher 2002).

Thermogravimetric analyses (TGA) of the treated SWCNTs were performed with a Q500 TA instrument under air, over a temperature range of 30-800 °C and a heating rate of 10 °C/min (around 4.5 mg samples in a platinum TGA pan).

3. Results and Discussion

3.1. Surface Characterization

3.1.1. X-ray Photoelectron Spectroscopy

We previously studied surface treatment of SWCNTs using PICVD and characterized the surface chemistry extensively by XPS (Hosseininasab et al. 2017). Briefly, the survey XPS spectra showed approximately 20% at. carbon (C), 20% at. iron (Fe) and 60% at. oxygen (O) on the surface (Fig. 2). Conversion of these values into weight

percentages leads to 46.7 wt% of Fe, 11.1 wt% of C, and 42.2 wt% of O. The surface chemistry (atomic percentage of functional groups) does not vary as a function of treatment time, for treatment times greater than 35 min, at which point the SWCNT surfaces were covered completely by the coating (Farhanian et al. 2017). This implies that an oligomeric coating with a surface atomic structure of "$C_nO_{3n}Fe_n$" deposited on the surface of SWCNT buckypapers. Farhanian et al. (2017) previously showed a linear relation between film thickness and treatment time in syngas/PICVD treatments, on a silicon substrate, with a deposition rate of 0.7 nm/min (for a total syngas flow of 400 mL/min, a residence time of 0.6 min, and treatments durations of 30-180 min) (Farhanian et al. 2017). Studying the high-resolution C1s peak, treated SWCNTs show four major functionalities compared to purified, untreated SWCNTs (P-SWCNTs): C-C, -OH, -COOH and carbonate groups with binding energies of 285, 286.7, 288.9, and 289.8 eV, respectively. As previously shown, the surface is completely and homogeneously covered by the coating (Hosseininasab et al. 2017). The O1s peak shows two peaks of interest at binding energies of 530 and 531.65 eV, assigned to O-Fe (or Fe_2O_3) and C-OH (or $Fe(OH)_3$), respectively (Vautard et al. 2012). The Fe2p peak confirms that Fe is in the form of Fe_2O_3, $Fe(OH)_n$ and Fe_3O_4 with subpeaks at binding energies of 710.55, 713.55, and 718.75 eV, respectively (Vautard et al. 2012).

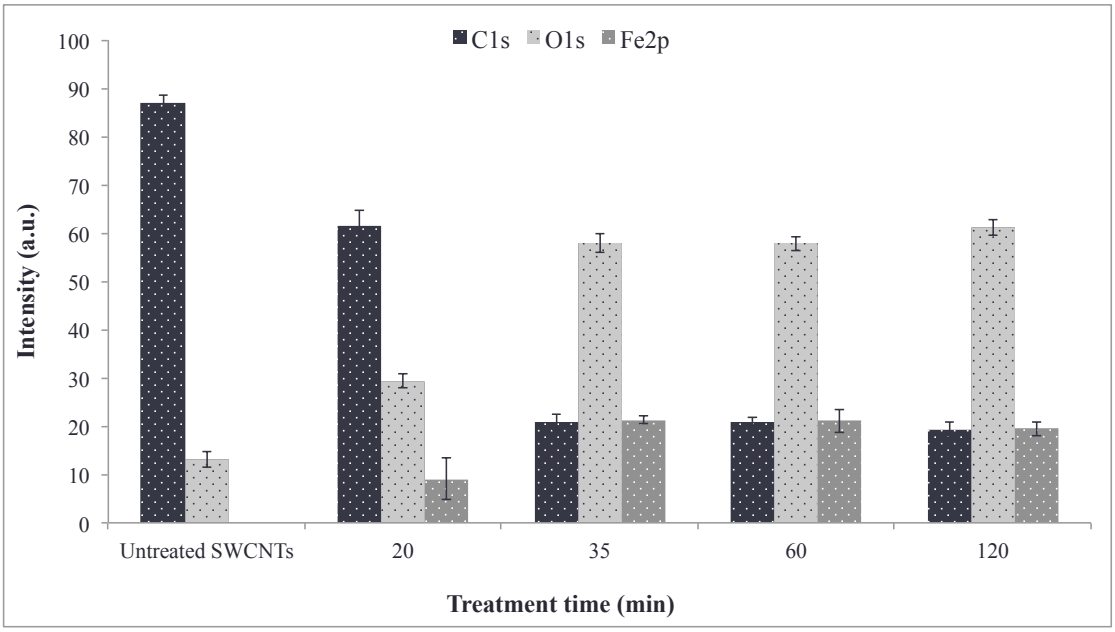

Fig. 2. Elemental surface composition of SWCNTs treated by PICVD without heating as a function of treatment time.

Temperature is a key thermodynamic parameter that can influence the surface chemistry of coatings (Andrzejewska 2001b; Mauron et al. 2002). Therefore, we varied the substrate temperature (both with and without UVC illumination, from 25 to 200°C) and assessed the surface composition via XPS (Fig. 3). From 100°C onwards (with the UVC lamps on), we never had complete surface coverage of the substrate, illustrated by the appearance of C=C bands from the SWCNT surface in high-resolution XPS scans (Fig. S2, supplementary results). The coating thickness was therefore either below the detection limit of the XPS (detection limit of XPS at most 10 nm) or completely absent in certain areas. In other words, the adsorption of reactive species is limited by rising temperature (thermal desorption) (Leach et al. 2002). Coating composition is generally similar, namely with respect to O-Fe and O-C functionalities, although oxygen-containing functionalities do increase with temperature (Fig. 4).

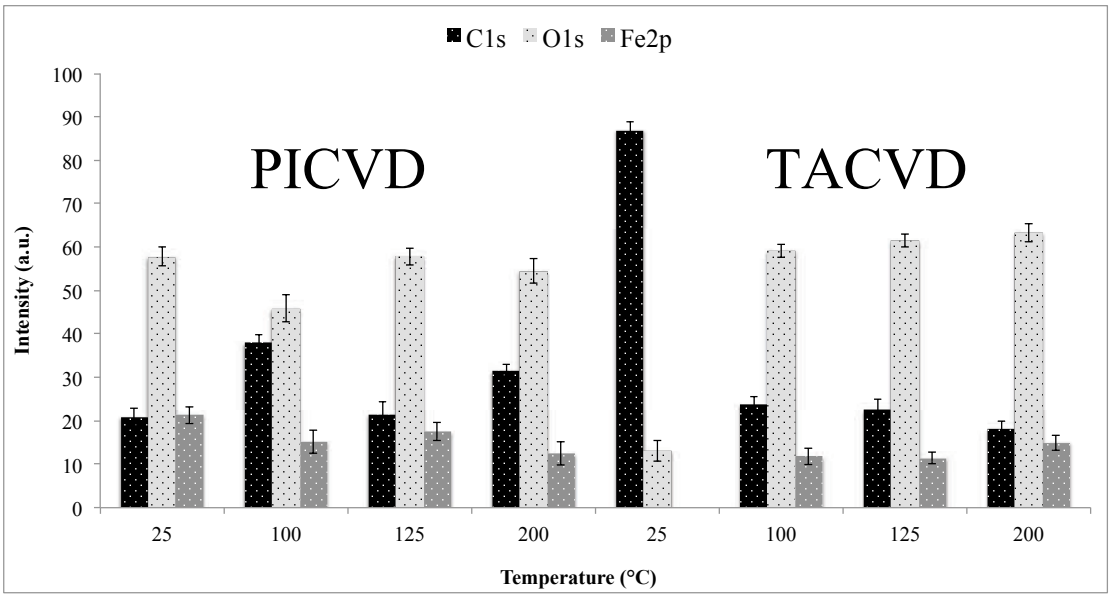

Fig. 3. Atomic percentage of carbon, iron and oxygen deposited on SWCNTs after PICVD (left) and TACVD (right) treatments at temperatures ranging from 25 to 200 °C.

When the UVC light is off (TACVD), the effect of temperature can clearly be assessed. At room temperature, there is no deposition (the elemental composition corresponds

directly to that of P-SWCNTs). Based on XPS survey scans, as temperature increases, C content decreases, while Fe increases. HR-XPS results showed that the preponderance of Fe functionalities (such as O-Fe) is greater than O-C functionalities - which is different from the case where heat is combined with UVC (Fig. S3, supplementary results) – and this is accentuated by increasing temperature. Based on an overlay of C1s HR-XPS (Fig. S3, supplementary results), TACVD treatments led to a coating with a higher content of oxygen-containing groups compared to PICVD (with or without heat), consistent with observations by (Fondell et al. 2015; Wang et al. 2013). This demonstrates that the heat- and light-driven decomposition pathways for $Fe(CO)_5$ are different. That being said, according to Fig. 3, a TACVD treatment at 200 °C, leads to an elemental surface composition close to that of room-temperature PICVD. The addition of heat is not without effect however – at temperatures higher than that of the thermal decomposition of $Fe(CO)_5$ (160°C) in the case of PICVD, coatings with different composition (more oxygen containing functionalities, especially COOH) compared to room-temperature PICVD were formed (Fig. 4). It is worth mentioning that after all UVC-based treatments, the PICVD reactor and SWCNT substrates became yellowish, while TACVD treatments did not lead to any color change.

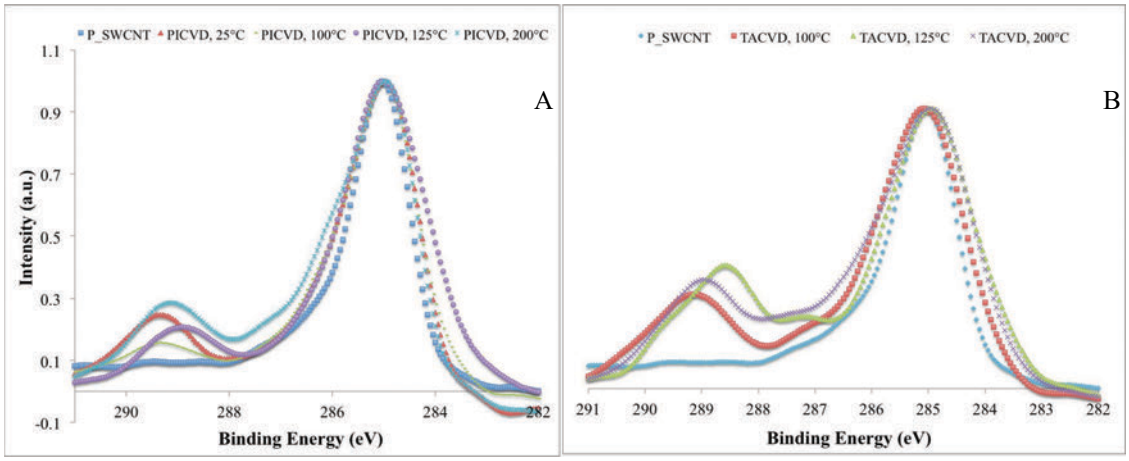

Fig. 4. HR-XPS C1s peak of (A) treated SWCNTs by PICVD at temperatures of 25, 100, 125, and 200 °C; (B) treated SWCNTs by TACVD at temperatures 25, 100, 125, and 200 °C while they are compared with (P-SWCNTs).

3.1.2. TGA Characterization

The deposits formed both with and without UVC illumination, at room temperature and at 200 °C, were quantified via TGA analyses. The data presented in Fig. 5 is extracted from the raw TGA and DTGA information presented in Fig. S4 in supplementary information. This interpretation, based on (Kim et al. 2009; Li et al. 2004), shows that a 4.51 mg samples of P-SWCNTs is composed of 3.43±0.11 mg C=C carbon (76.1±3.0% w/w, from the SWCNT structure), 0.42±0.03 mg humidity (9.5±0.8%, w/w) and 0.65±0.11 mg residue (14.5±2.9%, w/w). The residue is composed of graphitic C, soot and most importantly metallic species such as Fe (sourced in this case from the catalyst used for SWCNT growth (Bystrzejewski et al. 2008; Wang et al. 2004)). After PICVD treatment, SWCNT samples weighing 4.27 mg were composed of 1.98±0.04 mg C=C carbon (46.4±0.9%, w/w) and 1.64±0.03 mg residue (38.5±0.7%, w/w), with a new DTGA peak assigned to deposited C (in the form of C-C) accounting for 0.29±0.04 mg (6.7±1.0%, w/w) (remainder is humidity). In the absence of UVC light (TACVD), the treated SWCNT sample (3.09 mg) consisted of 1.37±0.03 mg C=C carbon (44.3±1.2%, w/w), 1.43±0.03 mg residue (46.3±1.1%, w/w) and only 0.24±0.02 mg deposited C (7.8±0.8%, w/w) (remainder humidity). To confirm that Fe (derived from iron pentacarbonyl) is responsible for the increased residual fraction measured after the various treatments, we characterized the residue using XPS. For PICVD samples, the residual fraction was composed of 10.0±1.4% at. Fe, 58.8±1.7% at. O and 31.2±0.3% at. C (graphitic C). Conversion of the atomic % of Fe to wt% gives the value of 30.0±1.4 wt%. Given the weight of the residue for treated SWCNTs samples (determined via TGA characterization, 1.64±0.03 mg), we can therefore calculate that the PICVD process was responsible for the addition of 0.49±0.03 mg of Fe. In other words, PICVD leads to a total deposition of 0.78±0.07 mg of C and Fe over 60 min, or a total deposition rate of 0.013±0.001 mg/min. Considering 10.0±1.4% at. deposited Fe (30.0±1.4 wt%. Fe) in the case of TACVD, 0.43±0.03 mg of Fe is deposited on the samples after 60 min treatment. Therefore, by taking the deposited mass of Fe (0.49±0.03 and 0.43±0.03 mg for PICVD and TACVD, repectively) and the related initial mass of analyzed samples (4.27 mg and and 3.09 mg of SWCNTs treated by PICVD and TACVD, respectively), 11.5% w/w of treated PICVD samples and 14% w/w of treated TACVD ones are consisted of Fe. This shows that TACVD leads to

coatings with more Fe rather than PICVD (the main component in the residue), also in agreement with the XPS findings, as well as previous works by (Fondell et al. 2015; Wang et al. 2013).

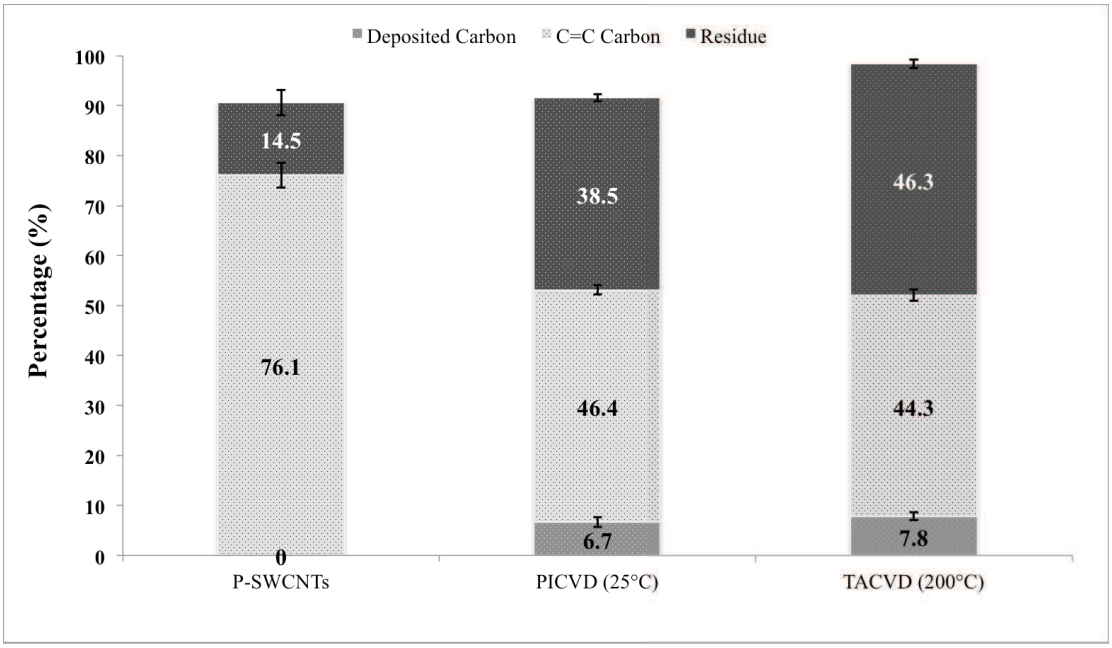

Fig. 5. TGA characterization of P-SWCNT and SWCNTs treated by PICVD.

3.2. Gas-Phase Characterizations

3.2.1. Fourier Transform Infrared Spectroscopy

Having confirmed that measurable deposits form on the surface of SWCNTs, we investigated the reaction products to better understand the PICVD process by using an on-line FTIR system connected to the reactor outlet. Argon and H_2 were fed to the reactor as control samples, as they are not expected to show any IR absorption (UVC lamps were inactive) (Fig. 6). When CO and H_2 are injected (UVC lamps inactive), the collected spectra showed two double peaks at wavenumbers of 2000/2050 cm^{-1} and 2100/2150 cm^{-1}, attributed to $Fe(CO)_5$ and CO, respectively (Tepe et al. 1999) . The fourth spectrum corresponds to syngas injection when the UVC light is on. As expected given its known photodissociation, activating the UVC light causes a decrease in the intensity of the $Fe(CO)_5$ peak. Upon injection of H_2O_2 (as a photo-initiator (PI) (El-Sheikh et al. 2010)), the $Fe(CO)_5$ peak almost completely disappears - this can be explained by the reaction of the remaining $Fe(CO)_5$ with the hydroxyl (OH) radicals

produced by photodissociation of H_2O_2 (Torrent et al. 1999). The FTIR results therefore corroborate consumption of $Fe(CO)_5$ under UVC light, and qualitatively show the effect of hydrogen peroxide during PICVD processing.

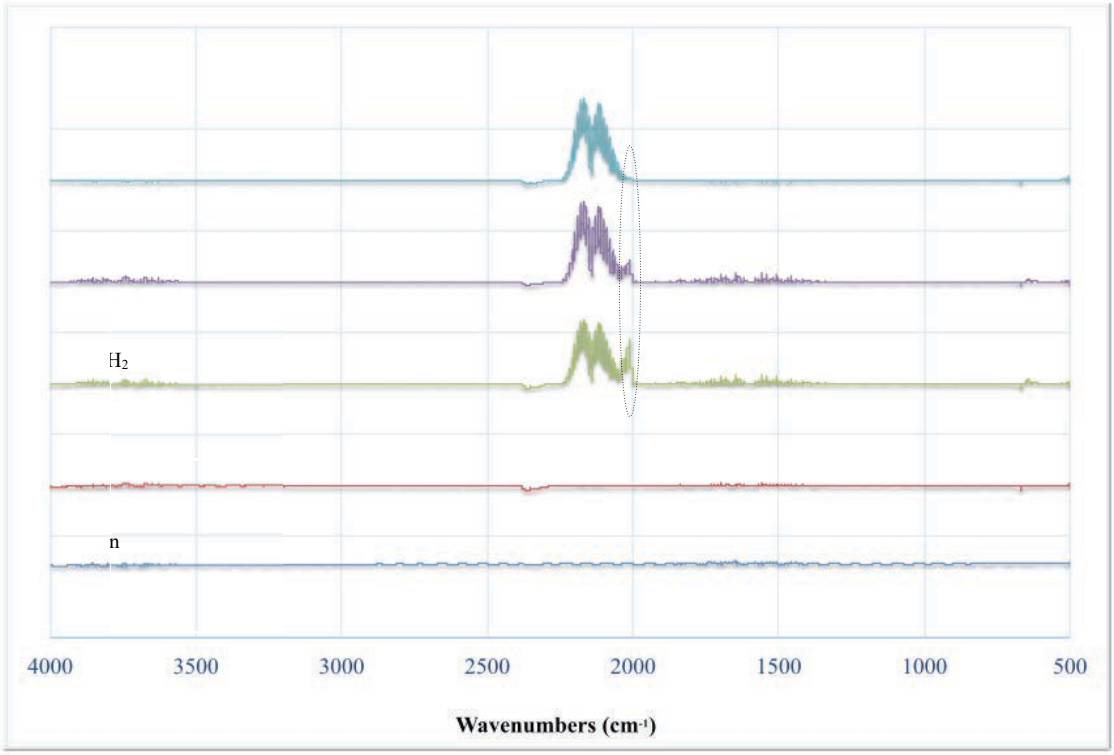

From bottom top, we present the outlet following the injection of Argon only, H_2 only, $CO+H_2$ (UVC lamp off) $CO+H_2$ (UVC lamp on), and finally $CO+H_2$ with H_2O_2 injection (UVC lamp on).

3.2.2. Gas Chromatography

Building upon the qualitative FTIR results, GC-MS was performed to identify and quantify the concentrations of chemical compounds at the inlet and outlet. Analysis at the PICVD reactor inlet (Fig. S5A in supplementary results) identified CO and $Fe(CO)_5$ as the sole products (90% match in the GC-MS library). These compounds had retention times of 9.4 and 1.22 min, respectively, and were identified using their mass spectra (with peaks at m/z = 56, 84 and 112 for $Fe(CO)_5$ and 12, 16 and 28 for CO). The same compounds were detected at the reactor outlet (Fig. S5B in supplementary results), but

with different concentrations since the UVC lamp was on. To quantify the consumption of gas species during PICVD treatment, the GC-MS was calibrated for CO, CO_2 and $Fe(CO)_5$ with two different columns (HayeSep N and Molsieve 5A columns). The calibration for $Fe(CO)_5$ was performed at concentrations of 0.1, 0.5 and 100 ppm in toluene. For CO and CO_2 quantification, calibration was performed using calibrating gas cylinders at purities of 1, 10 and 99.99%. Each concentration was analyzed at least three times by GC-MS to generate the calibration curves (see Fig. S1, S6A and S6B in supplementary results). Based on this calibration, the initial concentration of $Fe(CO)_5$ and CO at the reactor inlet were 6.7±0.2 ppm and 75±2%, respectively (Fig. 7A and 7B), when co-injecting CO, H_2 and H_2O_2. After a 20 min exposure to UVC light (with SWCNTs in the system), the concentrations of $Fe(CO)_5$ drops to 0.4±0.1 ppm, while CO remained relatively constant (any difference was below the detection limit of the instrument). In other words, 94±1% of the $Fe(CO)_5$ was consumed (which is reasonable given its strong absorption cross-section at the UVC lamps' peak emission (Liao and Gurol 1995)). When heating to 200 °C with UVC irradiation (also for 20 min), $Fe(CO)_5$ consumption did not change significantly (from 94±1% to 96±1%), in agreement with XPS results; CO also remains constant. If heating is applied independently (i.e. UVC lights remain off), the consumption of $Fe(CO)_5$ drops to 90±3% (i.e. final concentration of 0.7±0.2 ppm), with CO remaining unchanged (1h treatment time and total flow rate of 400 mL/min). Because GC-MS is unable to detect hydrogen, off-line micro GC was used. This analysis further serves to confirm the CO trends in GC-MS. At the inlet, CO and H_2 concentrations were 75±2% and 25±2%, respectively, while they were 75±2% and 25±2% at the outlet (Fig. 7C). In other words, gas-phase analysis showed no measurable consumption of CO and H_2 during the PICVD process (Berard et al. 2016; Dorval Dion et al. 2014; Hosseininasab et al. 2017; Labonté et al. 2016). Comparing the gas-phase characterizations with the previously described TGA results helps to clarify the roles of CO and H_2 and complete the mass balance. TGA analyses combined with XPS results showed that 0.49±0.20 mg of Fe and 0.29±0.04 mg of C were deposited onto the surface over the course of a 60 min PICVD treatment. Considering an inlet concentration of $Fe(CO)_5$ (6.7±0.2 ppm) in the CO stream (fed at 300 mL/min, the total number of moles over 60 min treatment: 850 µmol, 18.5 kPa, 25 ºC), the iron pentacarbonyl alone can account for a maximum of 47.3±1.4 mg of Fe, 50.9±1.5 mg of C, and 67.8±2.0 mg of O deposited within the entire reactor over the course of a 60 min

treatment (for every Fe atom present in the coating, 5 atoms of C and 5 atoms of O are deposited). Knowing that $Fe(CO)_5$ represents the sole source of Fe, and that 0.49±0.20 mg of Fe were deposited onto the SWCNT sample, this implies that approximately 1% of the inbound Fe is part of the coating. If we assume the same ratio applies to the C from $Fe(CO)_5$, then up to 0.53 mg of C could be traced back to that compound – this is greater than the amount of C actually deposited (0.29 mg), thus implying that $Fe(CO)_5$ is likely the sole source of C and Fe for deposition reaction and the CO fed to the reactor does not participate in the reactions. Even with the margin for error on the Fe estimate (±0.23 mg), this remains true for the lowest value of Fe.

Based on these findings and previously discussed FTIR results, we can infer that $Fe(CO)_5$ and H_2O_2 are the sole active contributors to the reaction. Further, measuring the weight of SWCNT buckypapers with a microbalance before and after treatment by PICVD revealed that 1.21 mg of coating was added to the surface over the 60 min reaction. Since 0.49 and 0.29 mg are already assigned to Fe and C, respectively, this leaves 0.43 mg for the O and H present on the surface. We can assume that O deposits in the same ratio as C sourced from $Fe(CO)_5$ (0.57%) onto the SWCNT sample, we can account for 0.39 mg. The remainder (0.04 mg) is sourced from H_2O_2 – assuming a 1:1 atomic ratio, 0.003 mg are H and 0.04 mg is O. In other words, the final surface composition is 0.29 mg of C (24 wt%, 24 µmol), 0.43 mg of O (35 wt%, 27 µmol), 0.49 mg of Fe (40 wt%, 9 µmol), and 2.35 µg of H (0.2 wt%, 3 µmol). This corresponds to an approximate atomic percentage composition of $C_{38}H_5O_{43}Fe_{14}$. This bulk chemical formula is different from the one obtained through near-surface analysis using XPS ($C_{21}O_{60}Fe_{19}$). The difference can be justified by a different structure of the bulk from the surface coating. It can be also assigned to the presence of unreacted radicals on the treated surfaces that can be oxidized upon the exposure to the air (Andrzejewska 2001a).

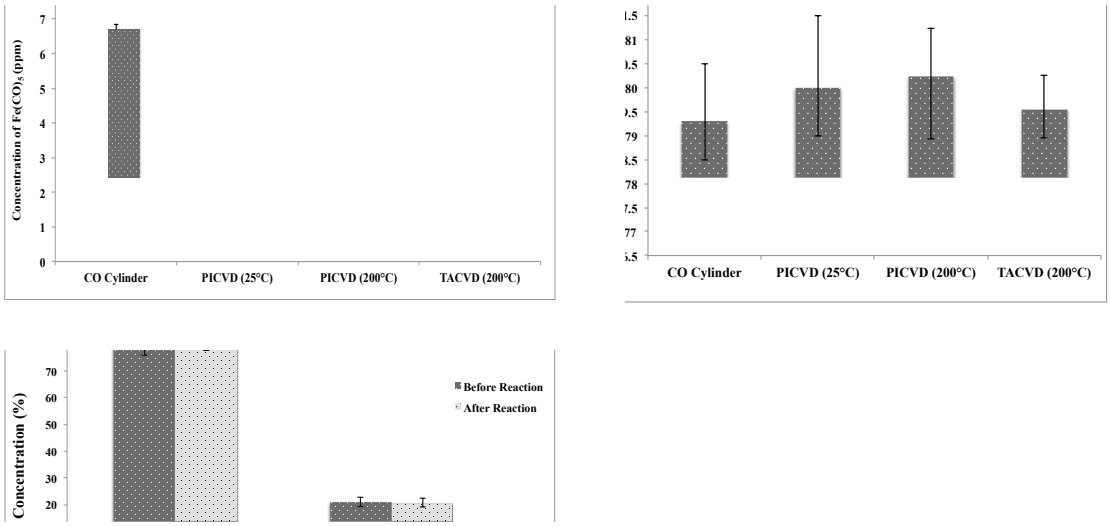

394

395 **Fig. 7.** Measured concentrations of A) $Fe(CO)_5$ obtained from GC-MS, B) CO obtained
396 from GC-MS , C) CO and H_2 obtained from micro GC.

397

398 **3.2.3. Concentration of $Fe(CO)_5$ Over Time**

399

400 The mass balance used to confirm the role of CO in the mechanism also identifies that
401 deposition occurs away from the SWCNT sample. This is apparent visually, as the
402 quartz tube reactor become more opaque over time, which can be measured by light
403 transmission through the tube (Fig. 8 inset). The decreased amount of light also means
404 that $Fe(CO)_5$ consumption decreases as a function of treatment time – the impact on

$Fe(CO)_5$ concentration at the reactor outlet becomes significant for treatment times longer than 30 min (Fig. 8). Therefore, reaction efficiency decreases over time during PICVD processing. It is interesting to note that there is no significant effect on $Fe(CO)_5$ decomposition for the first 20 min of treatment, despite a clear decrease in irradiance (Fig. 8 inset) – this implies that $2x10^{-4}$ W/cm^2 is sufficient energy for the $Fe(CO)_5$ decomposition reaction to move forward.

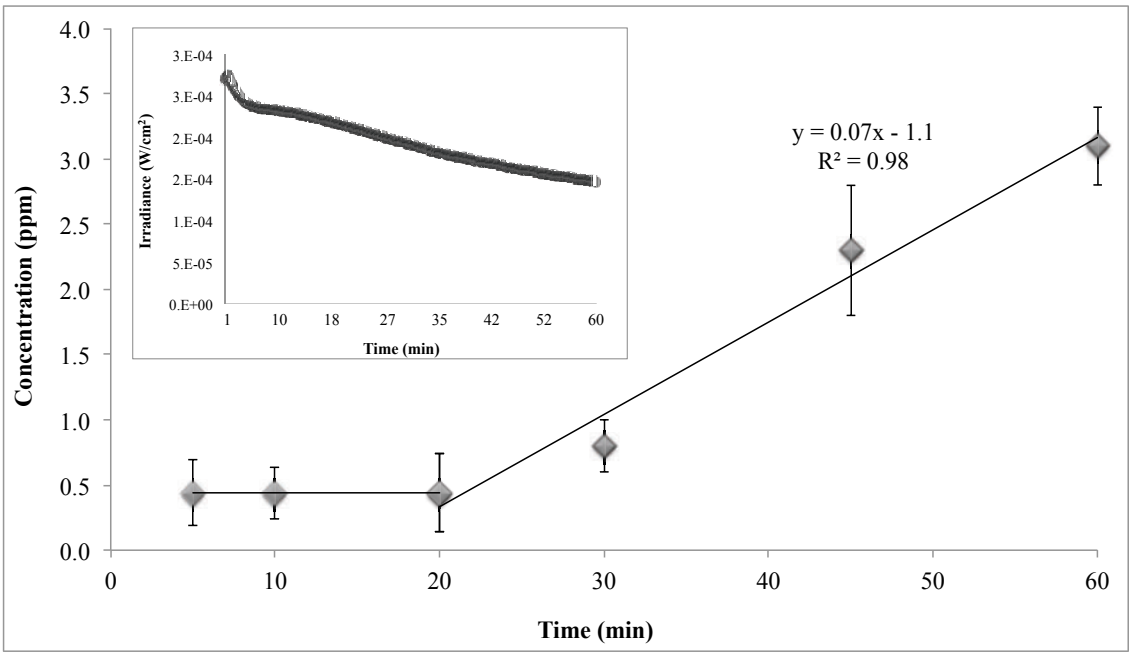

Fig. 8. Concentration of $Fe(CO)_5$ at the reactor outlet shown in Y axis versus treatment time in X axis. Inset: measured irradiance of UVC light during the PICVD process (Farhanian et al. 2017).

3.3. Kinetic Model

The kinetic model and proposed mechanism for PICVD in this study include both gas-phase and surface reactions focused on the decomposition of $Fe(CO)_5$ and H_2O_2 as the main precursors (Tables 1 and 2).

3.3.1. Gas-phase Reactions

According to the GC analysis, 94±1% of $Fe(CO)_5$ is consumed during PICVD processing (20 min treatment), in agreement with this compound's high absorption cross-section in the 200 to 350 nm range (overlapping with the UVC lamps' major emission peak at 253.7 nm) (Kotzian et al. 1989). As Seder et al. (1986) reported, the photo-dissociation pathway of this compound is sequential, from $Fe(CO)_4$ to $Fe(CO)_3$ and $Fe(CO)_2$ at 248 nm (very close to the present work, reactions G1-G3, Table 1) with corresponding reaction rate constants of $(3.5 \pm 0.9)\times10^{10}$, $(1.3 \pm 0.2)\times10^{13}$ and $(1.8 \pm 0.3)\times10^{13}$ Cm/mol.s (Seder et al. 1986a). The dissociation energies for $Fe(CO)_5$, $Fe(CO)_4$, $Fe(CO)_3$, $Fe(CO)_2$ Fe(CO), and Fe are reported to be around 56, 60, 91.5, 114.5 and 140 kcal/mol, respectively. A UVC light at 253.7 nm can provide energy equal to 112.5 kcal/mol (Poliakoff and Weitz 2002; Seder et al. 1986b). Therefore, except Fe(CO) and Fe, all other intermediates ($Fe(CO)_5$, $Fe(CO)_4$, $Fe(CO)_3$, $Fe(CO)_2$) can be formed in the reactor (reactions G1-G3, Table 1) (Poliakoff and Weitz 2002; Seder et al. 1986b). However, the UVC lamp also emits a secondary peak at 185 nm, which carries a photon energy of 155 kcal/mol. Therefore, it is possible to produce both Fe(CO) and Fe (Reactions G4 and G5, Table 1). Given H_2O_2's wide absorption range (180-340 nm), it can dissociate into two hydroxyl radicals ($OH^{\bullet}$) under UVC light (reaction G6, Table 1). According to the FTIR analysis, H_2O_2 injection increased $Fe(CO)_5$ consumption. This is evidence of the Fenton reaction, in which OH• radicals (formed from dissociation of H_2O_2) and $Fe(CO)_5$ react to form Fe• $(CO)_2OH$ and 3CO (reaction G7, Table 1) . Formed $OH^{\bullet}$ can then react with H_2O_2 to form $HO_2^{\bullet}$ radical and H_2O (reaction G8, Table 1). Further, $Fe(CO)_2$ can also react with the $OH^{\bullet}$ radical to form FeOH and 2CO (reaction G9, Table 1) (Castro et al. 1994). $CO^{\bullet}$ and H_2 can participate in chain reactions (reaction G10, Table 1) to produce $HCO^{\bullet}$ and $H^{\bullet}$ radicals. Carboxylic acid groups can be created by reacting CO and H_2O_2 (reaction G11, Table 1). Fe-containing intermediates can collide with each other to produce various iron oxide components in the gas phase, which subsequently deposit on the surfaces inside the reactor (reaction G12, Table 1).

Table 1. Proposed gas phase reaction mechanism for PICVD ($FeCO_5$+H_2O_2).

Samples	Reactions	*Ref.*
Decomposition of iron pentacarbonyl		
G1	$Fe(CO)_5 + \hbar\nu \leftrightarrow Fe(CO)_4 + C{\bullet}O$	*(Seder et al. 1986a)*
G2	$Fe(CO)_4 + \hbar\nu \leftrightarrow Fe(CO)_3 + C{\bullet}O$	*(Seder et al. 1986a)*
G3	$Fe(CO)_3 + \hbar\nu \leftrightarrow Fe(CO)_2 + C{\bullet}O$	*(Seder et al. 1986a)*
G4	$Fe(CO)_2 + \hbar\nu \rightarrow Fe\ (CO) + C{\bullet}O$	*(Nasri H. 2016)*
G5	$Fe(CO) + \hbar\nu \rightarrow Fe^* + C^{\bullet}O$	*(Nasri H. 2016)*
G6	$H_2O_2 + \hbar\nu \rightarrow 2OH^{\bullet}$	*(Chen et al. 2012)*
Free radical reactions		
G7	$Fe(CO)_5 + OH^{\bullet} \rightarrow Fe^{\bullet}(CO)_2OH + 3CO$	*(Liao and Gurol 1995)*
G8	$HO^{\bullet} + H_2O_2 \rightarrow HO_2^{\bullet} + H_2O$	*(Pignatello et al. 2006)*
G9	$Fe(CO)_2 + OH^{\bullet} \rightarrow FeOH + 2CO^*$	*(Chen et al. 2012)*
G10	$C^{\bullet}O + H_2 \rightarrow HC^{\bullet}O + H^{\bullet}$	*(Farhanian et al. 2017)*
G11	$C^{\bullet}O + H_2O_2 \rightarrow COOH^* + OH^{\bullet}$	*(Glarborg and Marshall 2009)*
G12	$Fe(CO)_2 + Fe(CO)_2 \rightarrow Fe_2(CO)_3 + C^{\bullet}O$	*(Wen et al. 2007)*

3.3.2. Surface Reactions

The surface reactions can be approximated as chemisorption and adsorption of the main gaseous species (H_2O_2, CO, $Fe(CO)_5$ and H_2) to the surface by passing through the boundary layer above the SWCNT substrate (reactions S1-S6, Table 2). Reaction S6 describes chemisorption of $OH^{\bullet}$ radicals which forms from the photo-dissociation of H_2O_2 in the gas phase participate in the radical chain reactions to form COOH and hydroxyl iron ($Fe(OH)_n$) derivatives through attachment to the free C/Fe sites on the surface (S20 and S29, Table 2). They also generate available free sites for the deposition of other reactive species via subsequent desorption of produced gases. After adsorption of reactive species and precursors, the mechanism continues by dissociation and excitation of adsorbed components (reactions S7 to S14, Table 2). We assume the same

photo-dissociation of $Fe(CO)_5$ to $Fe(CO)_4$, $Fe(CO)_3$, $Fe(CO)_2$, Fe(CO) and Fe, sequentially, occur on the surface as in the gas phase (reactions S7-S11, Table 2). The reaction of $Fe(CO)_5$ and $OH^{\bullet}$ radicals (Fenton reaction) leads to $Fe^{\bullet}(CO)_2OH_s$ and 3CO (reaction S12, Table 2). $CO^{\bullet}$ radicals detached from $Fe(CO)_5$ can deposit on available Fe, oxygen and carbon sites (Bradshaw and Hoffmann 1978; Brodén et al. 1979; Linsebigler et al. 1995). $CO^{\bullet}$ radicals can react with H_2 to produce $CH_2^{\bullet}/CO_2$ and $HCO^{\bullet}/H^{\bullet}$ radicals (reaction S13 and S14, Table 2). $Fe(CO)_2$ colliding with reactive species under UVC light leads to excited Fe (Fe*, reaction S15). The recombination reactions (or propagation steps) occur on the surface and various Fe components, such as Fe_{II}, Fe_{III}, FeCO, $Fe(OH)_3$, and Fe_2O_3, can be formed according to reactions S15-S21 (Table 2). In the propagation reactions, various hydrocarbon and $H^{\bullet}$ radicals can be formed through reactions S22 to S24 (Table 2). Reactive hydrocarbon species are assumed to adsorb onto both free sites on the SWCNT surface, and onto already adsorbed C species (Pan and Xing 2008). CO_2 and H radical can be obtained through reaction 25 (Table 2) in which termination happens by reacting $CO^{\bullet}$ and $OH^{\bullet}$ radicals. The collision of reactive species with each other terminates chain reactions, leading to various products such as FeOH, H_2O, COOH, CO, H_2, etc. on or near the SWCNT surfaces (reactions S26 to S29, Table 2). Film growth can continue through reaction S30 to present olefins and by the overall reactions (S1-S30) leading to metal-organic compounds with an overall chemical formula of $C_{24}H_3O_{27}Fe_9$ (Table 2).

Conclusions

In this study, we presented a kinetic model and reaction pathway for syngas PICVD based on both gas phase- and surface phase- characterizations. We also investigated the effect of temperature on PICVD as the main kinetic parameter for the first time and compared it with the results obtained from TACVD. The results showed that heat leads to a greater fraction of deposited Fe. While XPS results revealed the surface compositional structure of coating approximated as $C_{21}O_{60}Fe_{19}$ based on the atomic percentage (with mainly carboxylic, hydroxyl, $Fe(CO)_n$, and $Fe(OH)_n$ chemical moieties), TGA and gas-phase characterizations revealed a bulk coating structure of $C_{24}H_3O_{27}Fe_9$. A reaction scheme based on surface and gas phase reactions helps explain the appearance of the surface functional groups. GC-MS characterizations revealed the

significant effect of $Fe(CO)_5$ in the photochemical reaction: 94% is consumed and it is a major contributor to the oligomeric coating, though H_2O_2 also contribute, but to a lesser extent (only 0.016% of the H_2O_2 feed is deposited on ther surface). This points to a processing opportunity: if iron pentacarbonyl concentration can be controlled, it will be possible to do polymerization and significantly reduce CO and H_2 consumption compared to what was previously thought.

Table 2. Proposed surface reaction mechanism for PICVD ($FeCO_5$+H_2O_2) (*s* refers to oxygen, iron, and carbon free sites).

Samples	**Reactions**	**Ref.**
Adsorption and Desorption		
S1	$Fe(CO)_5 + s \leftrightarrow Fe(CO)_{5s}$	*n/a*
S2	$C^{\bullet}O + s \leftrightarrow C^{\bullet}O_s$	*n/a*
S3	$Fe^{\bullet}(CO)_2 + s \leftrightarrow Fe^{\bullet}(CO)_{2s}$	*n/a*
S4	$(CO)_2FeOH + s \leftrightarrow (CO)_2FeOH_s$	*n/a*
S5	$Fe_2(CO)_3 + s \leftrightarrow Fe_2(CO)_{3s}$	*n/a*
S6	$OH^{\bullet} + s \leftrightarrow OH_s$	*n/a*
Initiation		
S7	$Fe(CO)_{5s} + h\nu \rightarrow Fe(CO)_{4s} + C^{\bullet}O$	(Seder et al. 1986a)
S8	$Fe(CO)_{4s} + h\nu \rightarrow Fe(CO)_{3s} + C^{\bullet}O$	(Seder et al. 1986a)
S9	$Fe(CO)_{3s} + h\nu \rightarrow Fe(CO)_{2s} + C^{\bullet}O$	(Seder et al. 1986a)
S10	$Fe(CO)_{2s} + h\nu \rightarrow Fe(CO)_{s} + C^{\bullet}O$	(Nasri H. 2016)
S11	$Fe(CO)_{s} + h\nu \rightarrow Fe^{*}_{s} + C^{\bullet}O$	(Nasri H. 2016)
S12	$Fe(CO)_{5s} + OH \rightarrow Fe^{\bullet}(CO)_2OH_s + 3C^{\bullet}O$	(Chen et al. 2012)
S13	$2C^{\bullet}O + H_2 \rightarrow C^{\bullet}H_{2s} + CO_2$	(Farhanian et al. 2017)
S14	$C^{\bullet}O_s + H_{2s} \rightarrow HC^{\bullet}O_s + H^{\bullet}$	(Farhanian et al. 2017)
Propagation		
S15	$Fe^{\bullet}(CO)_{2s} \rightarrow Fe_s + 2C^{\bullet}O$	(Wen et al. 2007)
S16	$Fe_s^{\bullet} + Fe^{\bullet}(CO) \rightarrow Fe^{II}{}_s^{*} + C^{\bullet}O$	(Wen et al. 2007)

S17	$Fe^{II}_s + Fe(CO) \rightarrow Fe^{III}_s{}^* + C^{\bullet}O$	(Wen et al. 2007)
S18	$Fe^{II} + H_2O_2 \rightarrow Fe^{III} + OH^- + OH^{\bullet}$	(González-Davila et al. 2005)
S19	$Fe^{III} + H_2O_2 \rightarrow Fe^{II} + H^+ + HO_2^{\bullet}$	(González-Davila et al. 2005)
S20	$Fe^{III} + 3OH^{\bullet} \leftrightarrow Fe(OH)_{3s}{}^*$	(Majzlan et al. 2004)
S21	$2Fe(OH)_{3s} \rightarrow Fe_2O_{3s} + 3H_2O$	(Moreno C. et al. 2007)
S22	$HC^{\bullet}O_s + H_2 \rightarrow H_2C^{\bullet}O_s + H^{\bullet}$	(Farhanian et al. 2017)
S23	$C^{\bullet}H_{2s} + H_2 \rightarrow C^{\bullet}H_{3s} + H^{\bullet}$	(Farhanian et al. 2017)
S24	$C^{\bullet}H_3 + 2C^{\bullet}O \rightarrow CH_3CO + C^{\bullet}O$	(Farhanian et al. 2017)
S25	$C^{\bullet}O_s + OH^{\bullet} \rightarrow CO_2 + H^{\bullet}$	(Farhanian et al. 2017)
Termination		
S26	$Fe^{\bullet}(CO)_2 + OH^{\bullet} \rightarrow FeOH + 2CO$	(Farhanian et al. 2017)
S27	$2\ H_s{}^* \rightarrow H_2 + 2s$	(Ingle et al. 1996)
S28	$2\ OH^{\bullet}_s \rightarrow H_2O + s$	(Ingle et al. 1996)
S29	$C^{\bullet}O_s + OH^{\bullet} \rightarrow COOH_s$	(Kisacik et al. 2013)
S30	$n(C^{\bullet}O) + 2n\ (H_2) \rightarrow C_nH_{2n+1} + nH_2O$	(Farhanian et al. 2017)

ACKNOWLEDGMENTS

We wish to acknowledge the financial support provided by Fonds de recherche du Québec - Nature et technologies (FRQNT, grant no. 173942), as well as moral support from Polytechnique Montreal and Université de Sherbrooke. We would also like also to thank the Université de Sherbrooke Materials Characterization Laboratory, the Polytechnique Thin Films Group (GCM) and the microscopic characterization laboratory $(CM)^2$. Also, special thanks to Mohammad Jaber Darabi and Gregory S. Patience for their assistance in GC-MS characterizations. The authors are also grateful to Ms. Josianne Lefebvre for her support in XPS analysis.

References

Andrzejewska E (2001a) Photopolymerization kinetics of multifunctional monomers Progress in Polymer Science 26:605-665 doi:Doi 10.1016/S0079-6700(01)00004-1

Andrzejewska E (2001b) Photopolymerization kinetics of multifunctional monomers Prog Polym Sci 26:605-665 doi:Doi 10.1016/S0079-6700(01)00004-1

Berard A, Patience GS, Chouinard G, Tavares JR (2016) Photo Initiated Chemical Vapour Deposition To Increase Polymer Hydrophobicity Sci Rep 6:31574 doi:10.1038/srep31574

Bradshaw AM, Hoffmann FM (1978) The chemisorption of carbon monoxide on palladium single crystal surfaces: IR spectroscopic evidence for localised site adsorption Surf Sci 72:513-535

Brodén G, Gafner G, Bonzel HP (1979) Co adsorption on potassium promoted Fe(110) Surf Sci 84:295-314

Bystrzejewski M, Rummeli MH, Lange H, Huczko A, Baranowski P, Gemming T, Pichler T (2008) Single-walled carbon nanotubes synthesis: a direct comparison of laser ablation and carbon arc routes J Nanosci Nanotechnol 8:6178-6186

Castro M, Salahub DR, Fournier R (1994) A density functional study of FeCO, FeCO−, and FeCO+ J Chem Phys 100:8233-8239 doi:10.1063/1.466766

Chen Y, Zhang F, Xu C, Gao J, Zhai D, Zhao Z (2012) Theoretical investigation of water gas shift reaction catalyzed by iron group carbonyl complexes M(CO)5 (M = Fe, Ru, Os) J Phys Chem A 116:2529-2535 doi:10.1021/jp204776a

Choy KL (2003) Chemical vapour deposition of coatings Prog Mater Sci 48:57-170 doi:Pii S0079-6425(01)00009-3

Doi 10.1016/S0079-6425(01)00009-3

Dorval Dion CA, Raphael W, Tong E, Tavares JR (2014) Photo-initiated chemical vapor deposition of thin films using syngas for the functionalization of surfaces at room temperature and near-atmospheric pressure Surf Coat Technol 244:98-108 doi:10.1016/j.surfcoat.2014.01.043

El-Sheikh MA, Ramadan MA, El-Shafie A (2010) Photo-oxidation of rice starch. Part I: Using hydrogen peroxide Carbohydr Polym 80:266–269 doi:10.1016/j.carbpol.2009.11.023

Farhanian D, De Crescenzo G, Tavares JR (2017) Kinetics, Chemistry, and Morphology of Syngas Photoinitiated Chemical Vapor Deposition Langmuir 33:1780-1791 doi:10.1021/acs.langmuir.6b04151

Fondell M, Johansson F, Gorgoi M, von Fieandt L, Boman M, Lindblad A (2015) Phase control of iron oxides grown in nano-scale structures on FTO and Si(100): Hematite, maghemite and magnetite Vacuum 117:85-90 doi:10.1016/j.vacuum.2015.03.037

Girard-Lauriault PL, Illgen R, Ruiz JC, Wertheimer MR, Unger WES (2012) Surface functionalization of graphite and carbon nanotubes by vacuum-ultraviolet photochemical reactions Appl Surf Sci 258:8448-8454 doi:10.1016/j.apsusc.2012.03.012

Glarborg P, Marshall P (2009) The rate constant for the CO + H2O2 reaction Chem Phys Lett 475:40-43 doi:10.1016/j.cplett.2009.05.028

González-Davila M, Santana-Casiano JM, Millero FJ (2005) Oxidation of iron (II) nanomolar with H2O2 in seawater Geochim Cosmochim Acta 69:83-93 doi:10.1016/j.gca.2004.05.043

Hosseininasab S, Faucheux N, Soucy G, Tavares JR (2017) Inducing a Full Range of Wettability through Surface Modification of Single-Wall Carbon Nanotubes by Photo-Initiated Chemical Vapor Deposition Using Syngas Chem Eng J 325:101-113

Ingle NK, Theodoropoulos C, Mountziaris TJ, Wexler RM, Smith FTJ (1996) Reaction kinetics and transport phenomena underlying the low-pressure metalorganic chemical vapor deposition of GaAs J Cryst Growth 167:543-556 doi:10.1016/0022-0248(96)00277-1

Kasparek E, Tavares JR, Wertheimer MR, Girard-Lauriault P-L (2016) Sulfur-Rich Organic Films Deposited by Plasma- and Vacuum-Ultraviolet (VUV) Photo-Polymerization PLASMA PROCESS POLYM:n/a-n/a doi:10.1002/ppap.201500200

Kim KS, Imris M, Shahverdi A, Alinejad Y, Soucy G (2009) Single-Walled Carbon Nanotubes Prepared by Large-Scale Induction Thermal Plasma Process: Synthesis, Characterization, and Purification J Phys Chem C 113:4340-4348 doi:10.1021/jp810096k

Kisacik I, Stefanova A, Ernst S, Baltruschat H (2013) Oxidation of carbon monoxide, hydrogen peroxide and water at a boron doped diamond electrode: the competition for hydroxyl radicals Phys Chem Chem Phys 15:4616-4624 doi:10.1039/c3cp44643c

Kotzian M, Rosch N, Schroder H, Zerner MC (1989) Optical-Spectra of Transition-Metal Carbonyls - Cr(Co)6, Fe(Co)5, and Ni(Co)4 J Am Chem Soc 111:7687-7696 doi:DOI 10.1021/ja00202a004

584 Labonté V, Marion A, Virgilio N, Tavares JR (2016) Gas-Phase Surface Engineering of Polystyrene
585 Beads Used to Challenge Automated Particle Inspection Systems Ind Eng Chem Res 55:7362-
586 7372 doi:10.1021/acs.iecr.6b01573
587 Leach WT, Zhu JH, Ekerdt JG (2002) Thermal desorption effects in chemical vapor deposition of
588 silicon nanoparticles Journal of Crystal Growth 243:30-40 doi:Pii S0022-0248(02)01472-0
589 Doi 10.1016/S0022-0248(02)01472-0
590 Lee CJ, Park J, Huh Y, Lee JY (2001) Temperature effect on the growth of carbon nanotubes using
591 thermal chemical vapor deposition Chem Phys Lett 343:33-38 doi:Doi 10.1016/S0009-
592 2614(01)00680-7
593 Li F, Wang Y, Wang D, Wei F (2004) Characterization of single-wall carbon nanotubes by N2
594 adsorption Carbon 42:2375-2383 doi:10.1016/j.carbon.2004.02.025
595 Liao CH, Gurol MD (1995) Chemical oxidation by photolytic decomposition of hydrogen peroxide
596 Environ Sci Technol 29:3007-3014 doi:10.1021/es00012a018
597 Linsebigler A, Lu GQ, Yates JT (1995) Co Chemisorption on Tio2(110) - Oxygen Vacancy Site
598 Influence on Co Adsorption J Chem Phys 103:9438-9443 doi:Doi 10.1063/1.470005
599 Majzlan J, Navrotsky A, Schwertmann U (2004) Thermodynamics of iron oxides: Part III. Enthalpies
600 of formation and stability of ferrihydrite (~Fe(OH)3), schwertmannite
601 (~FeO(OH)3/4(SO4)1/8), and ε-Fe2O3 Geochim Cosmochim Acta 68:1049-1059
602 doi:10.1016/s0016-7037(03)00371-5
603 Mauron P, Emmenegger C, Zuttel A, Nutzenadel C, Sudan P, Schlapbach L (2002) Synthesis of
604 oriented nanotube films by chemical vapor deposition Carbon 40:1339-1344 doi:Pii S0008-
605 6223(01)00295-0
606 Doi 10.1016/S0008-6223(01)00295-0
607 Moreno C. HA, Cocke DL, Gomes JAG, Morkovsky P, Parga JR, Peterson E, Garciad C (2007)
608 Electrochemistry behind Electrocoagulation using Iron Electrodes ECS Transactions 6
609 Nasri H. FD, Boffito D.C., Patience G.S., De Crescenzo G., Chaouki J., Tavares J.R. (2016) Shedding
610 Light on Iron Pentacarbonyl Photochemistry Through A CVD Case Study submitted to
611 Chemical Communications
612 Nasri Lari H, Farhanian D, Boffito DC, Patience GS, De Crescenzo G, Chaouki J, Tavares JR (2017)
613 Shedding light on iron pentacarbonyl photochemistry through a CVD case study Catalysis
614 Communications 100:19-23 doi:10.1016/j.catcom.2017.06.024
615 P. J. Linstrom, Mallard WG (2001) NIST Chemistry WebBook; NIST Standard Reference Database
616 No 69
617 Pan B, Xing B (2008) Adsorption mechanisms of organic chemicals on carbon nanotubes Environ Sci
618 Technol 42:9005-9013
619 Pignatello JJ, Oliveros E, MacKay A (2006) Advanced oxidation processes for organic contaminant
620 destruction based on the Fenton reaction and related chemistry Crit Rev Env Sci Tec 36:1-84
621 doi:10.1080/10643380500326564
622 Poliakoff M, Weitz E (2002) Shedding light on organometallic reactions: the characterization of
623 tetracarbonyliron (Fe(CO)4), a prototypical reaction intermediate Acc Chem Res 20:408-414
624 doi:10.1021/ar00143a004
625 Raja M (2014) Surface Modification of Carbon Nanotubes with Combined UV and Ozone Treatments
626 FULLER NANOTUB CAR N 23:11-16 doi:10.1080/1536383x.2014.885960
627 Ruiz JC, Girard-Lauriault PL, Truica-Marasescu F, Wertheimer MR (2010) Plasma- and vacuum-
628 ultraviolet (VUV) photo-polymerisation of N- and O-rich thin films Radiat Phys Chem
629 79:310-314 doi:10.1016/j.radphyschem.2009.08.009
630 Seder TA, Ouderkirk AJ, Weitz E (1986a) The wavelength dependence of excimer laser photolysis of
631 Fe(CO)5 in the gas phase. Transient infrared spectroscopy and kinetics of the Fe(CO)x
632 (x=4,3,2) photofragments J Chem Phys 85:1977 doi:10.1063/1.451141
633 Seder TA, Ouderkirk AJ, Weitz E (1986b) The wavelength dependence of excimer laser photolysis of
634 Fe(CO)5 in the gas phase. Transient infrared spectroscopy and kinetics of the Fe(CO)x
635 (x=4,3,2) photofragments The Journal of Chemical Physics 85:1977 doi:10.1063/1.451141
636 Tepe RK, Vassallo D, Jacksier T, Barnes RM (1999) Iron pentacarbonyl determination in carbon
637 monoxide Spectrochim Acta B 54:1861 1868
638 Torrent M, Sola M, Frenking G (1999) Theoretical Study of Gas-Phase Reactions of Fe(CO)5 with
639 OH- and Their Relevance for the Water Gas Shift Reaction Organometallics 18:2801-2812
640 Vautard F, Ozcan S, Paulauskas F, Spruiell JE, Meyer H, Lance MJ (2012) Influence of the carbon
641 fiber surface microstructure on the surface chemistry generated by a thermo-chemical surface
642 treatment Appl Surf Sci 261:473-480 doi:10.1016/j.apsusc.2012.08.038

643 Wang P, Li HR, Du ZW (2013) Deposition of Iron on Graphite Felts by Thermal Decomposition of
644 Fe(CO)(5) for Anodic Modification of Microbial Fuel Cells Int J Electrochem Sc 8:4712-4722
645 Wang YY, Gupta S, Nemanich RJ (2004) Role of thin Fe catalyst in the synthesis of double- and
646 single-wall carbon nanotubes via microwave chemical vapor deposition Appl Phys Lett
647 85:2601-2603 doi:10.1063/1.1796529
648 Wen JZ, Goldsmith CF, Ashcraft RW, Green WH (2007) Detailed kinetic modeling of iron
649 nanoparticle synthesis from the decomposition of Fe(CO)(5) J Phys Chem C 111:5677-5688
650 doi:10.1021/jp066579q
651 Williams TC, Shaddix CR (2007) Contamination of Carbon Monoxide with Metal Carbonyls:
652 Implications for Combustion Research Combust Sci Technol 179:1225-1230
653 doi:10.1080/00102200601057279
654 Yang DQ, Sacher E (2002) s-p hybridization in highly oriented pyrolytic graphite and its change on
655 surface modification, as studied by X-ray photoelectron and Raman spectroscopies Surf Sci
656 504:125-137
657

SUPPLEMENTARY INFORMATION

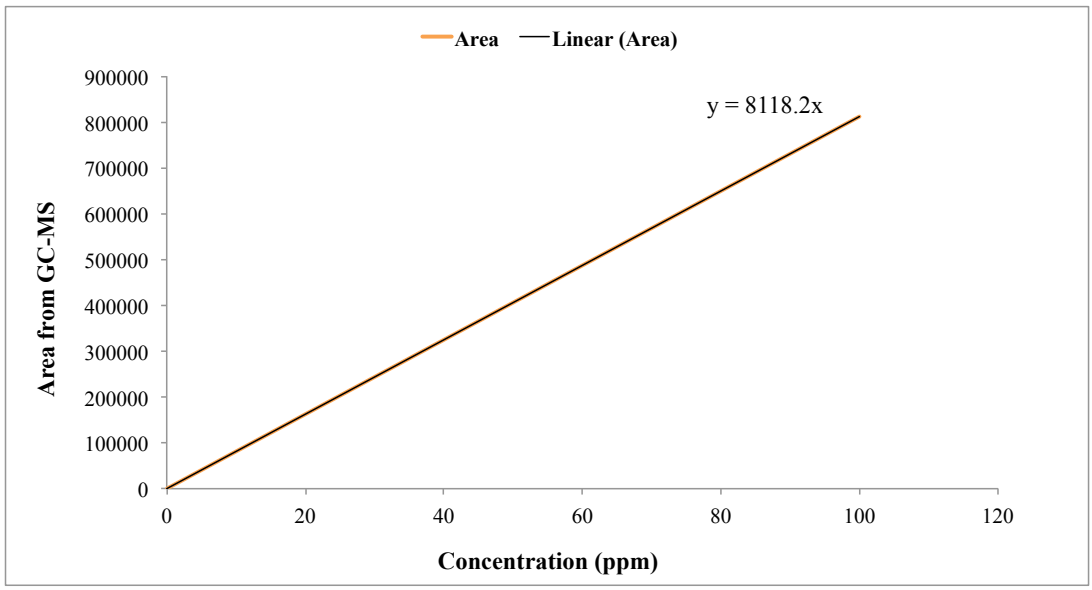

Fig. S1. Calibration curve of $Fe(CO)_5$ performed at concentrations of 0.1, 0.5 and 100 ppm in toluene.

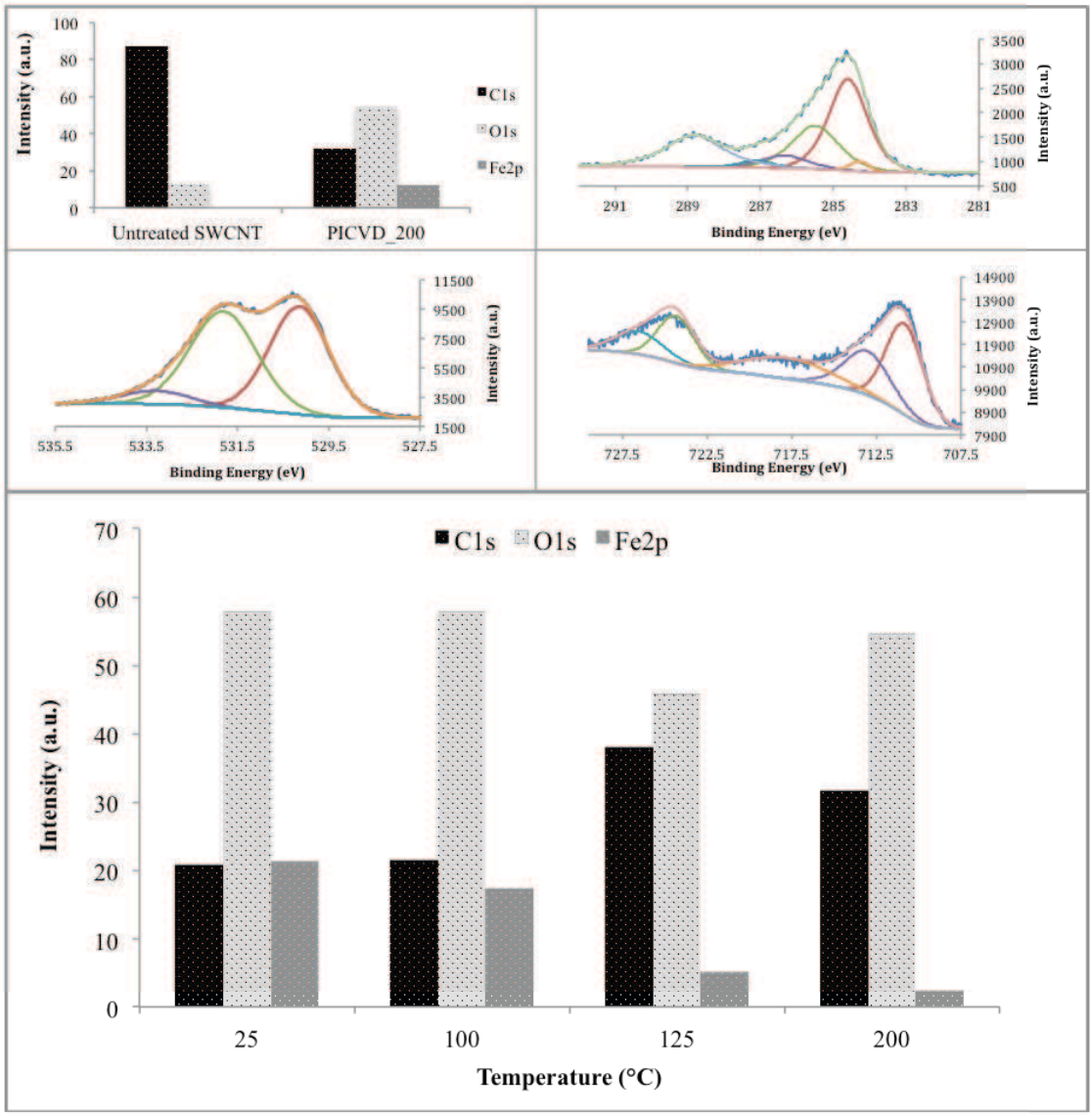

Fig. S2. A) Survey XPS spectra of treated SWCNT with syngas/PICVD_200 C, B) C1s HR-XPS of SWCNT treated with syngas/PICVD_200 C, C) O1s HR-XPS of SWCNT treated with syngas/PICVD_200 C, D) Fe2p HR-XPS of SWCNT treated with syngas/PICVD_200 C, E) Over plot of survey XPS spectra treated SWCNTs with syngas/PICVD over heat (the inset table is presenting the related numbers).

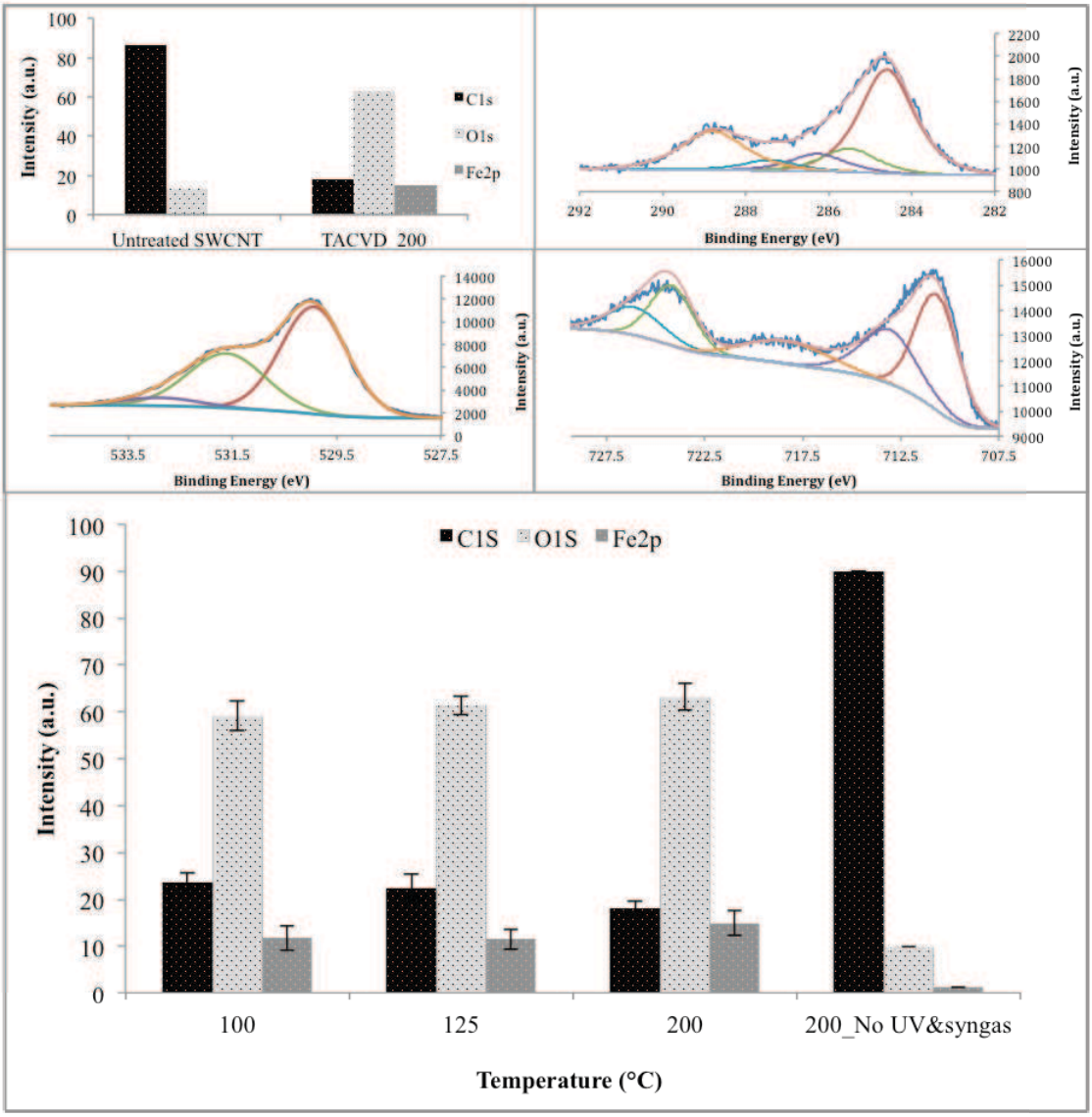

Fig. S3. A) Survey XPS spectra of treated SWCNT by syngas/TACVD_200 C, B) C1s HR-XPS of SWCNT treated by syngas/TACVD_200 C, C) O1s HR-XPS of SWCNT treated by syngas/TACVD_200 C, D) Fe2p HR-XPS of SWCNT treated by syngas/TACVD_200 C, E) Over plot of survey XPS spectra treated SWCNTs by syngas over heating (the inset table is presenting the related numbers).

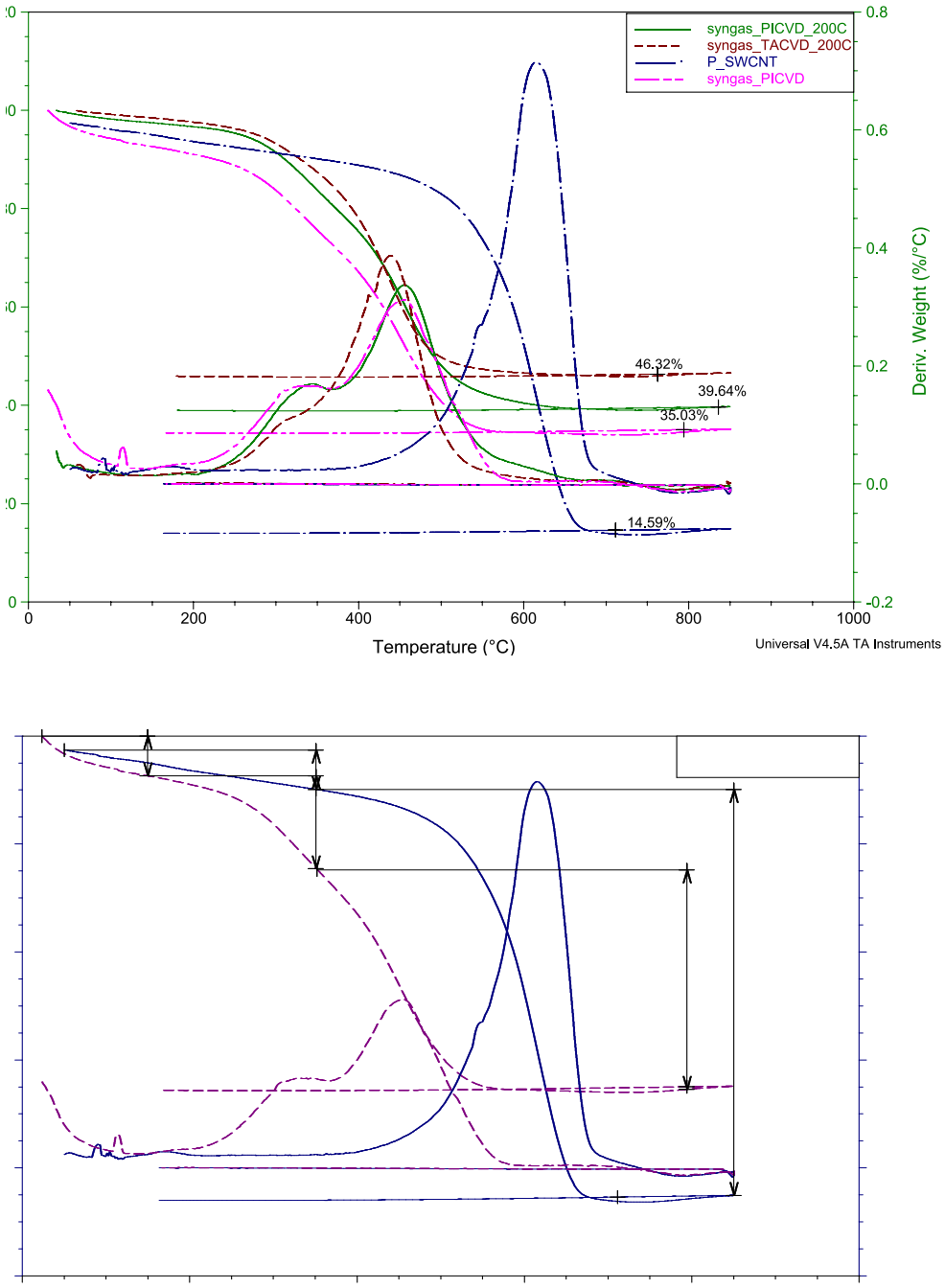

725

726 **Fig. S4.** A) Thermal decomposition analysis (TGA and DTG graphs) of P-SWCNTs,
727 PICVD, TACVD and PICVD over 200 ºC heating; B) Comparison of P-SWCNT and
728 PICVD treated SWCNTs in terms of thermal analysis.

729

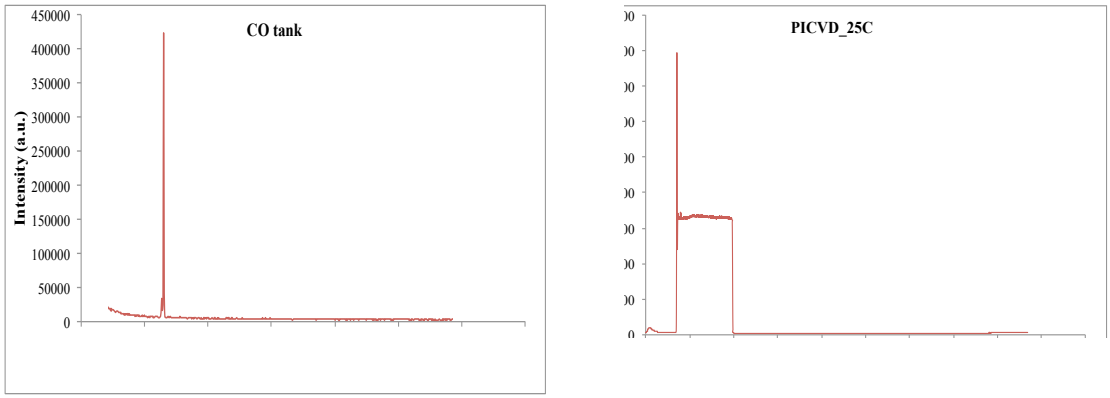

Fig. S5. GC-MS analysis of outlet gas of PICVD reactor A) before, and B) after syngas/PICVD reaction.

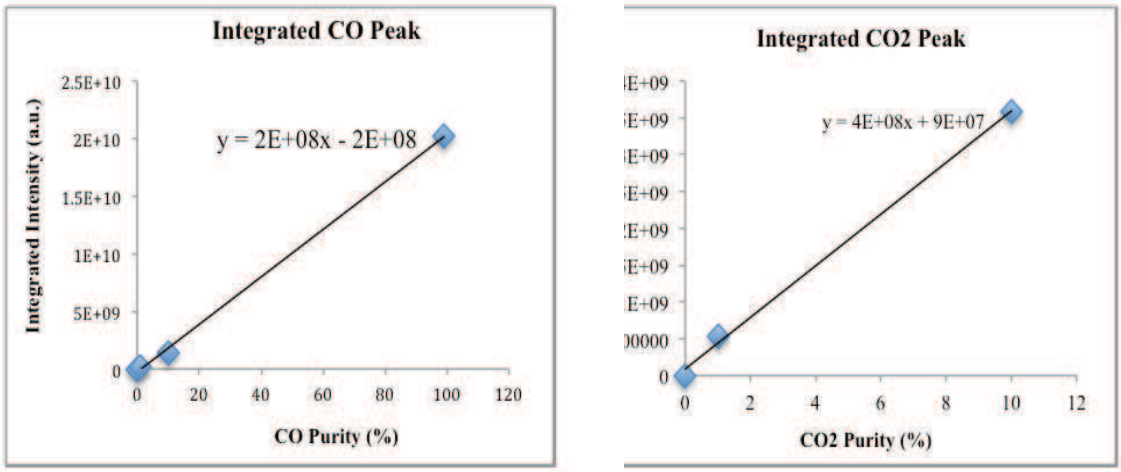

Fig. S6. Calibration curves of A) CO, B) CO_2 that performed according to calibrating gas cylinders at purities of 1, 10 and 99.99%.